TDDFT Studies of Absorption and SERS Spectra of Pyridine Interacting with Au_{20}

Christine M. Aikens and George C. Schatz*

Department of Chemistry, Northwestern University, Evanston, Illinois 60208-3113

Received: August 11, 2006; In Final Form: October 3, 2006

We present time dependent density functional theory (TDDFT) calculations for a tetrahedral Au_{20} complex interacting with pyridine for the purpose of modeling absorption and surface enhanced Raman scattering, with emphasis on chemical and electrodynamic enhancement effects. These calculations are done using the ADF code with the BP86 functional, the zeroth-order regular approximation and with the resonant electronic response modeled using a short time approximation expression for the perturbed density matrix, with a damping factor that is empirically chosen. The absorption spectrum of bare Au_{20} shows strong intraband (sp−sp) and interband (sp-d) coupling with a low-energy peak at 2.89 eV that is mostly intraband and other peaks at 3.94 and 4.70 eV that have mixed intra- and interband character. SERS spectra are calculated for pyridine/Au_{20} for both vertex (V) and surface (S) configurations at their respective lowest energy absorption maxima (near 2.89 eV), and we find that the V configuration has higher intensities that correspond to SERS enhancements of 10^3-10^4, whereas S has an enhancement of 10^2-10^3. These enhancement values are significantly lower than the analogous results for pyridine/Ag_{20} primarily because of reduced oscillator strength associated with the intraband transition in Au_{20}. Decomposition of the pyridine/Au_{20} enhancement factor into chemical and electromagnetic contributions (through an analysis of the static SERS intensities) shows enhanced chemical enhancements compared to Ag_{20} but reduced electromagnetic enhancements.

Introduction

Since the initial discovery of surface-enhanced Raman scattering (SERS) for pyridine on electrochemically roughened silver electrodes[1] and the subsequent recognition of the phenomenon,[2,3] SERS has become an important analytical tool due to its low detection limits, sensitivity to the molecular environment, highly enhanced vibrational signals, and good selectivity for adsorbates. The magnitude of the enhancement is affected by various factors such as the substrate material, surface roughness, and laser excitation wavelength, as well as other factors such as the solvent, electrochemical potential, coadsorbates, and nanoparticle/colloid aggregation. Typical SERS enhancements are of the order of 10^4-10^8, but enhancements of $10^{14}-10^{15}$ are possible and may facilitate single-molecule SERS.[4−6] Although the experimental conditions are highly complex, it is generally accepted that two primary mechanisms account for the sizable enhancement factors. The largest enhancements often arise from electromagnetic factors due to increased local fields near roughened surfaces, colloids, or nanoparticles as a result of plasmon resonance excitation, which is a collective excitation of the metal conduction electrons. In addition, chemical effects from metal-molecule charge-transfer excitations and other changes in the electronic properties of the molecule upon adsorption play an important role in SERS.

A number of metals besides silver have been suggested as being capable of producing SERS, including gold, copper, nickel, aluminum, iron, platinum, rhodium, ruthenium, cadmium, indium, and sodium. Although some of these metals can (at least at some wavelengths) exhibit strong free electron response that is analogous to that found for silver, and therefore can participate in plasmon mediated electromagnetic enhancement effects, others have strongly damped plasmons due to coupling to interband transitions, so significant electromagnetic enhancements are not expected. However, there are complicating factors in this assessment due to particle morphology effects, surface coverage effects, and "chemical" enhancement effects, so perhaps it is not surprising that there has been considerable confusion as to when the observed spectra should be properly labeled as SER spectra. As examples of this, a recent study suggests that some of the differences in SERS of aqueous pyridine adsorbed on silver, nickel, and cadmium surfaces versus gold, copper, and iron surfaces may be due to the formation of an α-pyridyl species on the latter three metals,[7] whereas other studies indicate that the Raman band shape is due to the strength of the molecule−metal bond.[8] A good understanding of the influence of the metal substrate on the chemical and electromagnetic enhancement mechanisms is critical for a more complete understanding of SERS.

Gold clusters have attracted considerable interest lately due to their potential technological applications. Single molecule electronics with gold nanowires show promise in the field of nanoelectronics.[9] The selective binding of thiolate-functionalized DNA to gold nanoparticles has initiated new methods of self-assembly.[10,11] Gold nanoparticles exhibit novel optical, electronic, and magnetic properties such as chiroptical activity in glutathione-passivated clusters.[12] Gold clusters also display a high resistance to oxidation.[13] In addition, small gold clusters on metal oxide supports have been found to be good catalysts for the oxidation of small molecules such as CO and H_2.[14,15] The structures of many of these clusters have been hotly debated, with planar structures established for the smallest gold clusters and three-dimensional structures predicted for the larger gold clusters (see refs 16−19 and references therein). Recent photoelectron spectroscopy and relativistic density functional calculations strongly predict that Au_{20} has a tetrahedral geometry similar to a fragment of bulk face-centered cubic (fcc) gold.[20]

* To whom correspondence should be addressed.

10.1021/jp065206m CCC: $33.50
Published on Web 11/16/2006

This similarity suggests the use of this cluster as a model of the bulk surface where each of the four faces of the tetrahedron represents a (111) surface. In addition, the apex and edge atoms have different coordination environments and may also provide useful sites for catalysis and other applications. Recently, a triphenylphosphine-stabilized Au_{20} cluster was synthesized in solution,[21] which highlights the current level of control over gold nanoparticles.

Electronic structure studies of molecules adsorbed on metal surfaces have the potential to elucidate the physical phenomena involved in SERS. Since electronic structure methods are limited by high computational demands, most previous SERS studies have used single metal atoms or small clusters to represent the metal surface.[8,22−28] Although most of these studies focused on static Raman intensities, a few previous investigations have used time-dependent Hartree Fock (TDHF) theory to treat dynamic Raman processes.[29,30] Other researchers have combined a polarizable dipole treatment of the metal with a TDHF evaluation of Raman intensities in order to examine the electromagnetic enhancements.[31]

The recent implementation of a short-time approximation[32] to the Raman scattering cross section within time-dependent density functional theory (TDDFT) enables the calculation of both normal and resonant Raman scattering intensities for molecules adsorbed on larger metal clusters than have been studied previously. This method has been used to examine the resonant Raman scattering for uracil,[33] pyrene,[33] and rhodamine 6G,[34] as well as the surface enhanced Raman scattering of pyridine on a tetrahedral Ag_{20} particle[35] and of pyrazine at the junction of two Ag_{20} clusters.[36] For pyridine/Ag_{20}, the calculations suggest that SERS enhancement factors of 10^5 are possible, which shows that SERS is not limited to larger nanoparticle systems, in spite of the expected damping of plasmon excitation in small clusters due to electron scattering from the particle surfaces. For small silver clusters, the optically bright state is not a true plasmon excitation, as it is dominated by few electron transitions. However resonance Raman scattering involving this state produces enhanced Raman scattering in the adsorbed pyridine due to electromagnetic coupling between pyridine and the cluster. Chemical contributions to the enhancement are also possible, so the TDDFT calculations provide useful mechanistic information that relates closely with the true SERS process.

In this work, we examine the physical phenomena that result when pyridine is adsorbed on gold (represented by the Au_{20} cluster). Gold provides significant challenges compared to the earlier work on silver due to important relativistic effects that cause strong interactions between conduction band and interband transitions. However, despite the challenge, the ability to do theoretical studies of gold is important for a number of reasons. Gold nanoparticles exhibit free electron response and therefore plasmon enhanced Raman scattering at long wavelengths and then highly damped response due to interband transitions and no significant SERS activity at short wavelengths. Small gold clusters have well-defined structures and well-characterized coordination chemistry as noted above, and although the SERS activity of small gold clusters is unknown, there have been several studies of other optical properties of size-selected clusters, so there is a body of data that can be used for calibration. Our studies in this paper will focus on Au_{20}, as this has a well-defined structure and only two high-symmetry coordination sites. We will use pyridine as the adsorbate, as this has often been used for SERS work, and comparisons with earlier TDDFT studies of pyridine/Ag_{20} will provide an important calibration for the present calculations.

Computational Details

All calculations discussed in this work were performed with a local version of the Amsterdam Density Functional (ADF) 2005.01 program.[37] The molecular structures of the species studied were calculated at the density functional (DFT) level of theory using the gradient-corrected Becke-Perdew (BP86) exchange-correlation functional[38,39] because this functional often yields harmonic frequencies that are close to experimental values.[40] A triple-ζ with polarization functions (TZP) Slater type basis set was utilized with a [$1s^2$-$4f^{14}$] frozen core for Au and a [$1s^2$] frozen core for the first row elements. The zeroth-order regular approximation (ZORA) was employed in the calculations to account for the scalar relativistic effects.[41] Calculations were run using the highest molecular symmetry possible for each structure (T_d for Au_{20}, C_{2v} for pyridine, and C_s for the metal−pyridine complex). The SCF convergence was tightened to 10^{-8}. A gradient convergence criterion of 10^{-4} and an energy convergence criterion of 10^{-5} were used in order to obtain well-converged geometries. Frequencies were calculated numerically. A list of the optimized geometries and harmonic frequencies for each structure considered in this work is given in the Supporting Information.

Excited states were calculated using time-dependent DFT (TDDFT). The tolerance was set to 10^{-8}, and the orthonormality was set to 10^{-10}. (Further information about these technical parameters is available in the online ADF manual.)[42] For Au_{20}, only electronic transitions from the ground state to singlet T_2 excited states are dipole allowed, so only singlet−singlet excitations to these states were evaluated for the optical absorption spectrum. A total of 150 states were examined for the metal cluster, whereas 600 states were examined for the metal−pyridine complex. For the Au_{20} spectrum corresponding to photodetachment, 600 singlet and triplet states were considered.

The real and imaginary polarizabilities were computed using the AORESPONSE module[43] and a short-time approximation to evaluate the perturbed density matrix (and from this the frequency dependent polarizability).[32] A damping parameter of $\Gamma = 0.0037$ a.u. (which is determined by the dephasing time of the conduction electrons) was previously found to be reasonable for modeling the absorption spectra of silver clusters.[32,35] We have used this same value for consistency in this study, which should be reasonable for the conduction electron response given that silver and gold have nearly the same Drude width. A less certain issue in this calculation is the treatment of the damping of interband transitions. Although damping is expected to be stronger for these transitions, limitations of the code we have used have forced us to use the same damping parameter for all excited states. We will assess the influence of this approximation in our analysis below.

In the TDDFT calculations, the numerical integration accuracy of integrals for the Fock matrix elements and energy terms was increased to 10^{-8}. The adiabatic local density approximation (ALDA) was used in all polarizability calculations. Polarizability derivatives were calculated by numerical differentiation with respect to the normal mode displacements.

As in ref 35, differential Raman scattering cross sections are presented in this work. These are calculated by

$$\frac{d\sigma}{d\Omega} = \frac{\pi^2}{\epsilon_0^2}(\omega - \omega_p)^4 \frac{h}{8\pi^2 c\omega_p}[45\bar{\alpha}'_p{}^2 + 7\gamma'_p{}^2]\frac{1}{45(1 - \exp(-hc\omega_p/k_B T))} \quad (1)$$

where $45\bar{\alpha}'_p{}^2 + 7\gamma'_p{}^2$ is the scattering factor, $\bar{\alpha}'_p$ and γ'_p are the isotropic and anisotropic polarizability derivatives with respect to the *p*th vibrational mode, respectively, and ω and ω_p are the frequencies of the incident radiation and the *p*th vibrational mode, respectively. The polarizabilities consist of both real $\alpha^R_{\alpha\beta}(-\omega;\omega)$ and imaginary $\alpha^I_{\alpha\beta}(-\omega;\omega)$ components, which can be expressed by[32]

$$\alpha^R_{\alpha\beta}(-\omega;\omega) = \sum_{n\neq i,f} \frac{\langle f|\mu_\alpha|n\rangle\langle n|\mu_\beta|i\rangle(\omega_{ni} - \omega)}{(\omega_{ni} - \omega)^2 + \Gamma^2} + \frac{\langle f|\mu_\alpha|n\rangle\langle n|\mu_\beta|i\rangle(\omega_{nf} + \omega)}{(\omega_{nf} + \omega)^2 + \Gamma^2} \quad (2)$$

$$\alpha^I_{\alpha\beta}(-\omega;\omega) = \Gamma\sum_{n\neq i,f} \frac{\langle f|\mu_\alpha|n\rangle\langle n|\mu_\beta|i\rangle}{(\omega_{ni} - \omega)^2 + \Gamma^2} + \frac{\langle f|\mu_\alpha|n\rangle\langle n|\mu_\beta|i\rangle}{(\omega_{nf} + \omega)^2 + \Gamma^2} \quad (3)$$

where Γ is the damping parameter, μ_α is the dipole moment operator, and *i*, *f*, and *n* are the initial, final, and intermediate (virtual) states, respectively.

Results and Discussion

Au_{20} Excitation Spectra. The inclusion of scalar relativistic effects has a dramatic impact on the structure of Au_{20}, whereas this has a negligible impact for Ag_{20}. The calculated optical absorption spectrum of tetrahedral Ag_{20} consists of a single peak at 3.5 eV, which is created by a strong sp intraband transition. When scalar relativistic effects are considered, the oscillator strength is reduced by 40% compared to nonrelativistic calculations.[44] For Au_{20}, the average Au−Au bond length is 2.775 Å, which is a decrease of 0.177 Å or 6% compared to a nonrelativistic calculation. Furthermore, the consideration of relativistic effects in gold clusters has critical consequences for the optical absorption spectrum as a result of the alterations in the orbital energies. For a single gold atom in a nonrelativistic calculation, the energy difference between the 6s and 5d orbitals is 3.965 eV. After scalar relativistic effects are included, this energy difference is predicted to be 1.190 eV. As a result, the d orbitals are better able to mix in the excitation spectrum.

The electronic structure of the Au_{20} cluster is characterized by a filled d band that slightly overlaps a group of sp hybrid orbitals. The sp orbitals include both the highest occupied molecular orbital (HOMO) and the lowest unoccupied molecular orbital (LUMO). A set of predominantly p type orbitals appears at higher energies. The excitation spectrum (shown in Figure 1) may be decomposed into contributions from sp−sp intraband transitions, sp−d interband transitions, p−sp interband transitions, and p−d interband transitions. The sp−d transitions form a broad background in the spectrum. The low-energy excitations are dominated by sp−sp intraband transitions, although the sp−d transitions also play a role. The first significant maximum in the theoretical spectrum occurs at 2.893 eV, which is in good agreement with the measurements reported by Collings et al. for various gold clusters.[45] These results also qualitatively agree with a previously reported spectrum for Au_{20} that was calculated using the LB94 functional,[46] although the LB94 spectrum may slightly overestimate the excitation energies, and a previously reported spectrum that was computed using the BP86 functional with the LANL2DZ effective core potential basis set.[47]

Experimental studies of gold clusters reinforce the trends observed in this work. The optical absorption spectra for Au_n-

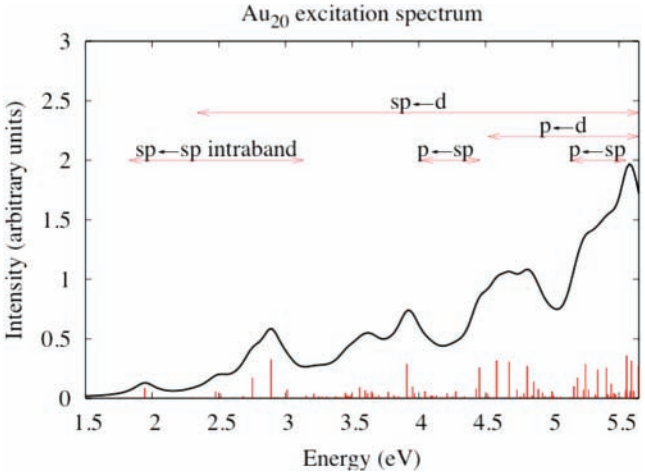

Figure 1. Calculated optical absorption spectrum of the tetrahedral Au_{20} cluster. The peaks are broadened by a Lorentzian with a half-width of 0.2 eV.

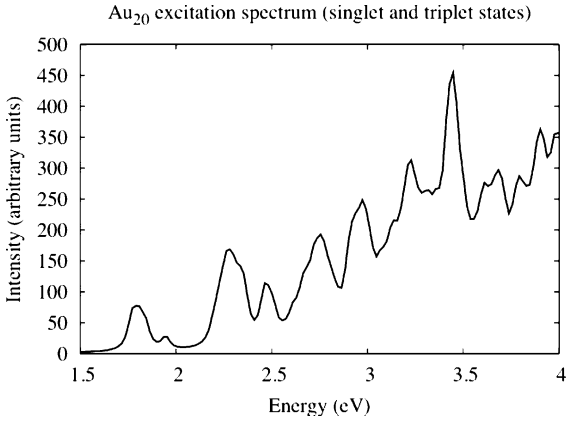

Figure 2. Calculated Au_{20} excitation spectrum relevant to photodetachment spectroscopy. The distribution of excited singlet and triplet states is fit with unit-area Lorentzian functions with a half-width of 0.05 eV.

Xe_m and $Au_nXe_m^+$ (n = 7, 9, 11, and 13 and m = 1 and 2) show a lowest energy peak near 2.9 eV (for the higher *n* values) that is blue-shifted with respect to the plasmon peak at 2.4 eV that one finds for 10 nm gold particles or which is calculated according to Mie theory.[45] The blue shift is thought to reflect the effect of electron "spill-out" on the conduction band energies of the surface Au atoms (all of the atoms in these clusters are surface atoms), as this leads to weaker coupling of the conduction and interband transitions. The results in ref 45 for higher *n* also show strong absorption at energies above 2.9 eV, including a broad peak near 3.8 eV that matches our peak at 3.9 eV. There is also strong absorption above 37 000 cm^{-1} (4.6 eV),[45] but the agreement with our peak at 4.7 eV is less apparent.

In photodetachment studies, measurement of the kinetic energy of an electron ejected from an anionic species yields information about the relative energies of the ground and excited singlet and triplet states. The transition is not restricted by symmetry selection rules because the ejected electron can carry any necessary angular momentum to make the process electric dipole allowed. Experimental photodetachment studies of the Au_{20}^- anion predict the gap between the ground state singlet and first excited triplet state to be 1.77 eV.[20,48] In addition, large peaks can be noted at energies corresponding to 2.2, 2.7, and 3.1 eV above the ground state.[20,48] These peaks are well-reproduced by the theoretical spectrum shown in Figure 2.

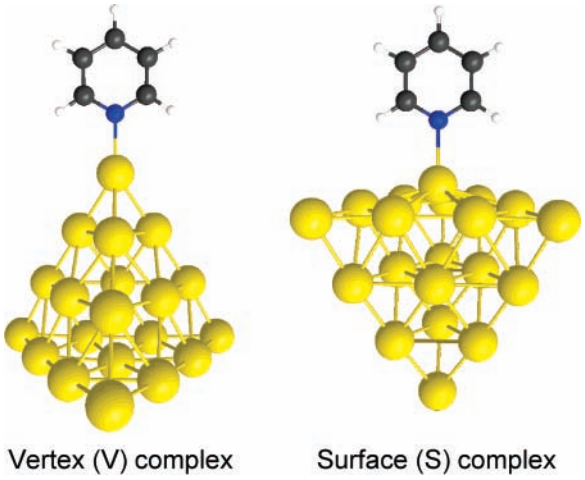

Figure 3. Configurations of the two C_s pyridine−Au_{20} complexes considered in this study.

TABLE 1: Calculated Bond Distances, Binding Energies, and Charge Transferred from the Metal to the Pyridine (Based On VDD Charges) for Pyridine−M_{20} Complexes (M = Ag or Au)

complex	bond distance (Å)	binding energy (kcal/mol)	charge transferred (electrons)
pyridine−Au_{20} (vertex)	2.23	−17.13	0.27
pyridine−Au_{20} (surface)	2.33	−5.54	0.20
pyridine−Ag_{20} (vertex)[a]	2.46	−9.19	0.13
pyridine−Ag_{20} (surface)[a]	2.66	−1.99	0.11

[a] Reference 35.

Pyridine−Au_{20} Ground State Properties. As discussed in the Introduction, the Au_{20} cluster may be viewed as a fragment of the fcc lattice of bulk gold. Two of the possible binding modes to this cluster include binding to a vertex atom (denoted the V-complex), which can represent an adatom site, and binding to one of the four faces (denoted the S-complex), which can represent binding to the (111) surface. These two configurations are shown in Figure 3. For each complex, the binding energy, bond length between the N atom and the closest gold atom, and electronic charge transferred from the metal cluster to the pyridine are shown in Table 1. As for silver, the binding interaction for the V-complex is stronger than that for the S-complex. The binding interaction for both binding sites is stronger when the pyridine interacts with gold rather than silver, as may be expected.[8] The electronic charge transferred to the pyridine is slightly greater for gold than for silver based on calculating the Voronoi deformation density (VDD) charges. These charges are computed by spatial integration of the electron density function over an atomic domain and have similar values to Hirshfeld charges.[49]

Charge-Transfer Bands in Excitation Spectrum. For gold, the involvement of the d-electrons increases the intricacy of the excitation spectra for the V- and S-complexes (Figures 4 and 5) compared to the corresponding spectra for Ag. The presence of a pyridine molecule near a metal cluster or surface may result in new charge-transfer (CT) excitations from the metal to the molecule. Transitions that are composed of at least 80% CT character (defined as an excitation from occupied orbitals in the metal cluster to unoccupied orbitals on the pyridine molecule) are shown as solid red lines. Transitions with 25−80% CT character are denoted by dotted blue lines. The remaining transitions, which are composed principally of metal−metal excitations, are represented by dashed grey lines. For the

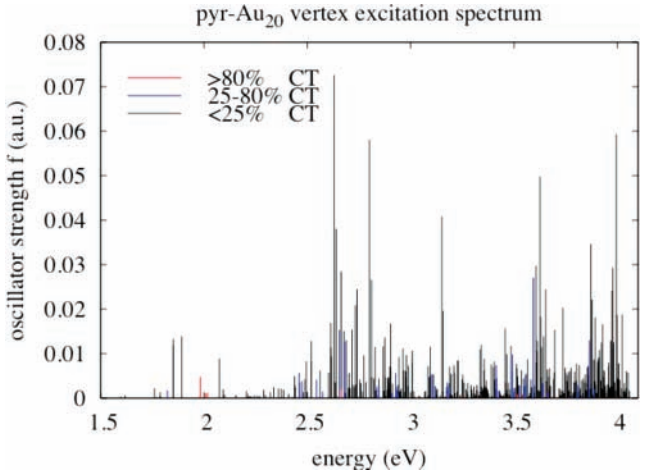

Figure 4. Calculated optical absorption spectrum of the V-complex.

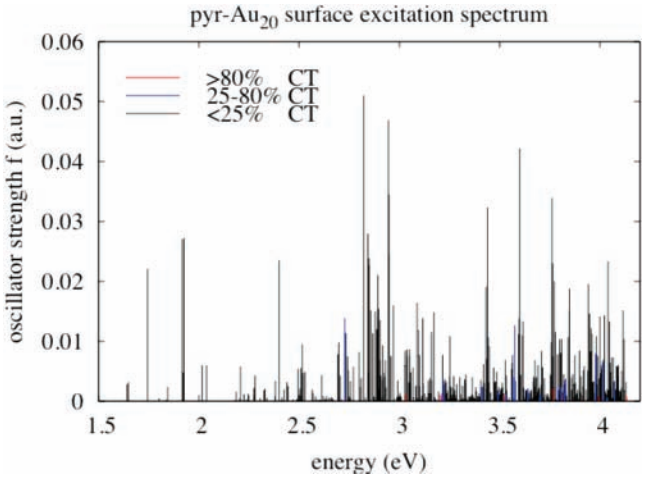

Figure 5. Calculated optical absorption spectrum of the S-complex.

V-complex, four CT excitations are predicted between 1.97 and 2.02 eV with oscillator strengths from 0.001 to 0.005 a.u. The remaining CT excitations are almost entirely hidden by metal−metal transitions. For the S-complex, no CT excitations are predicted to lie in regions of the spectrum away from metal−metal transitions. It should be stated that DFT is known to underestimate the excitation energies for long-range CT states in weakly interacting complexes due to incorrect asymptotic behavior of approximate exchange−correlation functionals (i.e., the self-energy error);[50] thus, it is possible that the CT excitations will occur at higher energies where they would be further hidden by metal−metal transitions. In general, these calculations suggest that the experimental observation of CT bands for the pyridine−Au_{20} system will be challenging.

Using the transient reflecting grating (TRG) method, Sawada et al. suggest the existence of charge-transfer transitions between 500 and 650 nm (1.9−2.5 eV) for the pyridine−gold system, particularly at the longer wavelengths, based on increased decay times for the TRG signals of the pyridine-adsorbed roughened SERS active substrate than the nonactive substrate.[51] In fact, these predicted transitions would be close to the calculated charge-transfer states at ∼2 eV for the vertex (adatom) structure (Figure 4). This could also support the idea that certain adsorption sites facilitate charge-transfer.

Polarizability Maxima for Complexes. For a given system, the magnitude of the isotropic imaginary polarizability is proportional to the excitation spectrum. The first major maximum in the excitation spectrum occurs around 2.7 eV for the

V-complex and 2.9 eV for the S-complex (Figures 4 and 5). This maximum in the V-spectrum is significantly red-shifted (~0.2 eV) from the Au_{20} cluster maximum at 2.89 eV. The maxima in the imaginary polarizability for the V- and S-complexes occur at 464 nm (2.67 eV) and 429 nm (2.89 eV), respectively.

Enhanced Raman Scattering. *Static Raman Scattering Spectra.* The static Raman scattering spectra can be used to characterize the chemical component of the SERS enhancement mechanism, as enhancements in the static intensities arise from physical phenomena such as changes in the electronic properties of molecules and charge-transfer excitations that arise from molecule−metal interactions. The static Raman spectra for gas-phase pyridine and the vertex and surface orientations of the pyridine−Au_{20} complex are shown in Figure 6. The pyridine cross section is calculated assuming an excitation wavelength of 514.5 nm in the prefactor of eq 1 but with $\omega = 0$ in the scattering factor and is of the order of 10^{-32} cm^2/sr. The pyridine/Au cross sections are also calculated assuming an excitation wavelength of 514.5 nm in the prefactor of eq 1 and are of the order of 10^{-30} and 10^{-31} cm^2/sr for the vertex and surface complexes, respectively. The effects on the pyridine spectrum due to incorporation of the scalar relativistic effects are negligible (for comparison, see Figure 5a in ref 35). Two intense modes at 977 and 1021 cm^{-1} dominate the spectrum. The modes at 1572, 1566, and 1205 cm^{-1} also have significant intensity.

Upon complexation to the metal cluster, the frequencies of several modes shift significantly. For the V-complex, the largest changes are blue shifts of 17, 22, and 26 cm^{-1} for the pyridine modes at 1572, 977, and 599 cm^{-1}. For the S-complex, these modes are blue-shifted by 13, 17, and 19 cm^{-1}, respectively. These modes have a_1 symmetry, and the latter two have significant vibrational motion along the N−Au bond. For silver, the former two modes are shifted by 13 and 14 cm^{-1} for the V-complex and by 8 and 10 cm^{-1} for the S-complex. The larger mode shifts for the gold V-complex than for the gold S-complex and the silver complexes can be associated with the greater strength of the bonding interaction (Table 1). These findings agree with previous results for monatomic[26] and diatomic[25] pyridine complexes.

The intensity enhancements are determined from the scattering factor. For the V-complex, the intensities of the most intense Raman modes increase by about a factor of 20 compared to the gas phase intensities; the enhancements vary from about a factor of 3 for the mode at 1025 cm^{-1} to a factor of 55 for the mode at 1589 cm^{-1}. In contrast, chemical enhancement effects for the V-complex of pyridine on silver result in an intensity enhancement of about 8.[35] This may again be due in part to the stronger chemical bonding of pyridine to gold. For the gold S-complex, the intensities are enhanced by about a factor of 3, which is similar to that found for silver.[35]

For the V-complex, the relative enhancement of the 999 cm^{-1} peak is much greater than the enhancement of the 1021 cm^{-1} peak for the gold substrate compared to the silver substrate. In addition, the peak at 624 cm^{-1} is more pronounced. For the S-complex, the chemical enhancement of the 1021 cm^{-1} peak is greater than the enhancement of the 994 cm^{-1} peak, although the differences between the gold and silver spectra are slight. A peak at 860 cm^{-1} is pronounced in the gold spectrum, whereas the peak at 607 cm^{-1} is not visible. Overall, the vertex orientation exhibits a greater sensitivity to the substrate, which results in strong chemical enhancement effects for the pyridine-Au_{20} V-complex.

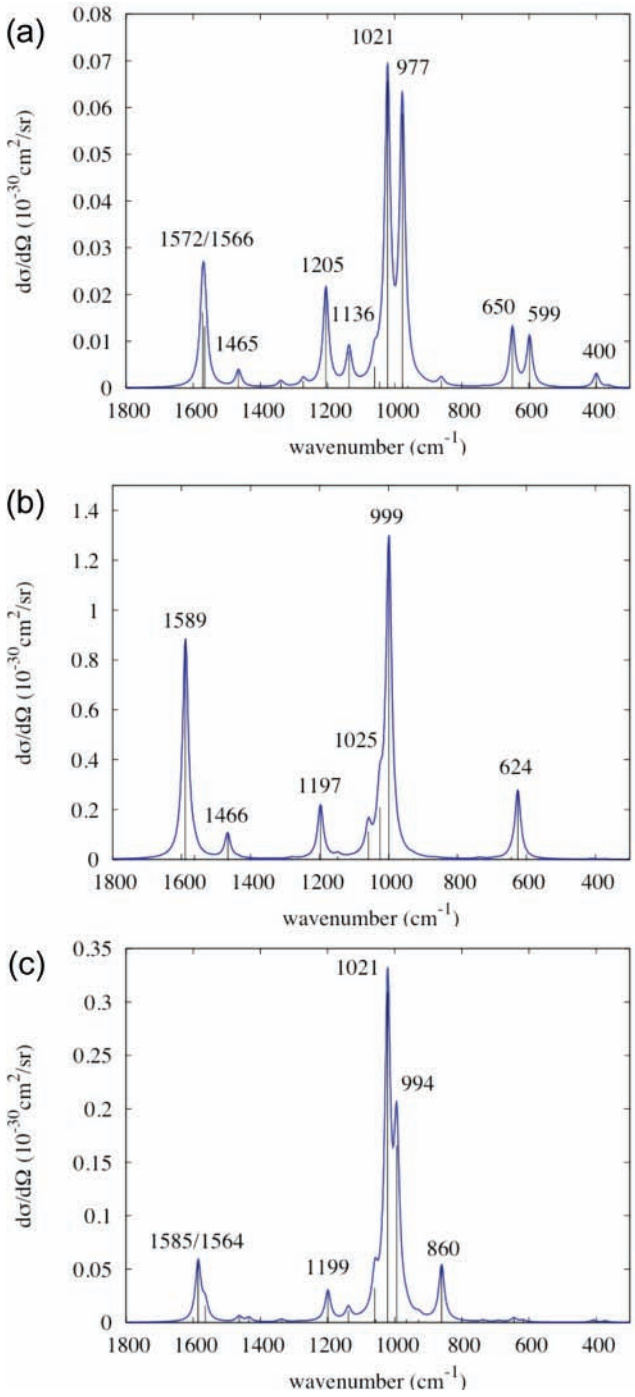

Figure 6. Calculated static Raman spectra of (a) pyridine and the (b) vertex and (c) surface pyridine−Au_{20} complexes.

Resonant Raman Scattering. Resonance between excitations in the metal and the incident field leads to electromagnetic contributions to the Raman enhancement in addition to the chemical enhancement that determines the static spectrum. In the resonant Raman scattering calculations, the excitation wavelengths were chosen to correspond with the maxima in the imaginary polarizability for the V- and S-complexes (464 and 429 nm, respectively). The cross sections are of the order of 10^{-28} and 10^{-29} cm^2/sr, which correspond to overall enhancements of 10^3-10^4 and 10^2-10^3 for the V- and S-complexes, respectively (Figure 7). For the V-complex, an electromagnetic enhancement of 10^2-10^3 may be roughly estimated by dividing the overall enhancement factor by the chemical enhancement factor of 20. For the S-complex, the

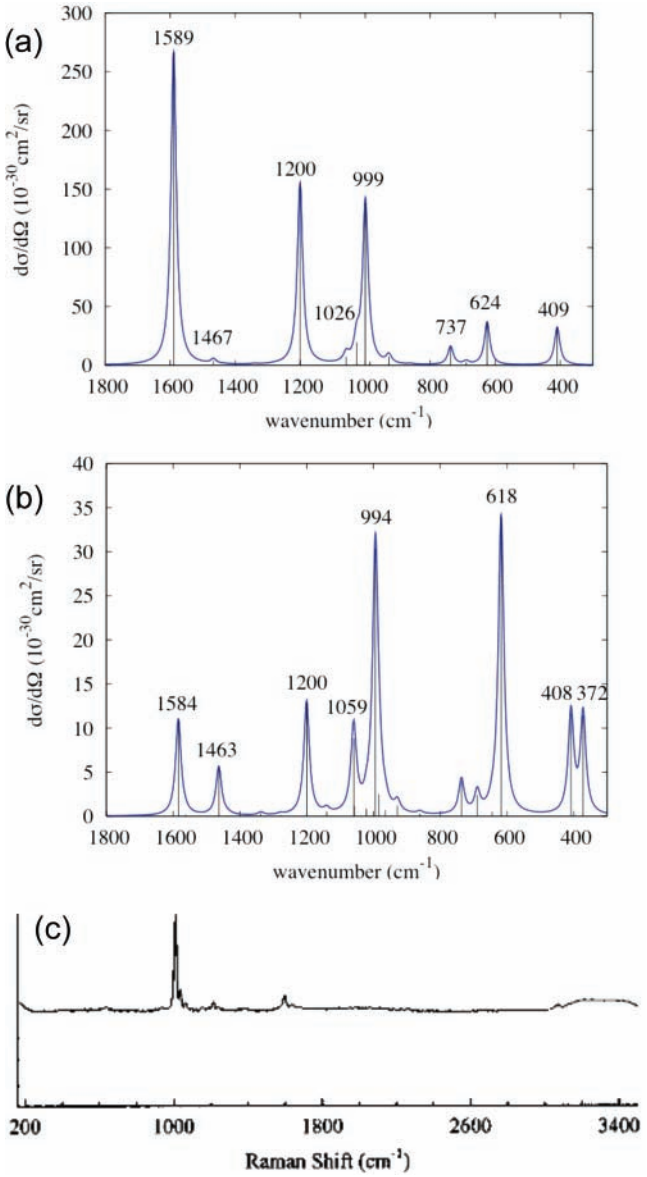

Figure 7. Calculated resonant Raman spectra of pyridine−Au_{20} (a) vertex and (b) surface complexes. (c) Experimental SERS spectrum of pyridine on gold from ref 7.

electromagnetic enhancement is predicted to be of the order of 10^2. The overall enhancement factors for the gold complexes are less than the corresponding overall enhancement factors for silver. For the V-complex, the reduction in the enhancement factor is 1 order of magnitude compared to the values reported in ref 35.[52] When scalar relativistic results are included, the enhancement factor for silver is reduced by an order of magnitude,[44] so the two metals have similar enhancements for the V-complex. For the S-complex, the enhancement factor is reduced by 2 orders of magnitude relative to scalar relativistic results for the silver. As a consequence, the gold cluster enhancement factors are smaller for the S-complex than for the V-complex, whereas the opposite is true for the silver cluster.

For the V-complex, the modes at 1589 and 1200 cm^{-1} are enhanced relative to the mode at 999 cm^{-1} in the resonant Raman calculations. The trigonal ring breathing mode at 1026 cm^{-1} continues to have a small intensity relative to the 999 cm^{-1} symmetric ring breathing mode. For the S-complex, the intensity of the 1021 cm^{-1} trigonal ring breathing mode decreases relative to the 994 cm^{-1} symmetric ring breathing mode. In addition, the intensity of the mode at 618 cm^{-1} becomes significant.

The experimental Raman spectrum of pyridine on a roughened gold substrate exhibits an intense peak at 1013 cm^{-1} for the totally symmetric ring breathing mode, whereas the peaks at 1597 and 1213 cm^{-1} are less intense than this mode (Figure 7c).[7] In the predicted spectrum for the V-complex (Figure 7a), the peaks at 1589 and 1200 cm^{-1} are stronger than the peak at 999 cm^{-1}, which is the opposite to what is seen in the roughened gold substrate experiments. In fact, the experimental spectrum seems more like the spectrum of the S-complex (Figure 7b), which could be an indication that a larger proportion of binding sites yield S-complexes than V-complexes. Thus, it is possible that S-complexes dominate the experimental spectrum. However, even the S-complex spectrum is not a perfect match with the experimental results, as the peaks at 1463, 1059, and 618 cm^{-1} are significantly over-estimated by the calculations.[7] These differences may be due to the use of a Au_{20} cluster rather than a roughened gold surface, and we also note that the measurements refer to much high surface coverage than we have studied. Coverage effects could lead to pyridines that are not as strongly interacting with the surface as we have modeled, leading to an observed spectrum which is more like that of gas-phase pyridine.

Excitation Wavelength Dependence. One difference between the resonant Raman scattering calculations for Au_{20} (this work) and Ag_{20} (ref 35) relates to the excitation wavelength at which the calculations are performed. Whereas the silver cluster has a single strong excitation at 3.44 eV due to an intraband transition, the gold cluster has a more complicated absorption spectrum. Although the first substantial maximum occurs at 2.89 eV and corresponds to a collective intraband transition in analogy to the silver cluster, other maxima in the computed gold absorption spectrum fall at higher energies (3.94 and 4.70 eV) and have greater intensities. These other maxima involve mixed intraband and interband excitation, so it is of interest to determine if the enhancements are larger or smaller than for the pure intraband excitation that was considered in Figure 7. In making these comparisons, however, we should note that the damping factor was assumed to be the same for both intraband and interband transitions, so possibly larger damping associated with interband transitions is not included.

At the absorption maximum for the silver V-complex (3.42 eV/363 nm), the oscillator strength for the gold V-complex is less than the oscillator strength at its first maximum at 2.67 eV, although the absorption cross sections have the reverse ordering due to the higher frequency of the 3.42 eV excitation. We find that the Raman scattering factors vary as the square of the oscillator strength, with that at 363 nm being approximately a factor of 0.65 times the scattering factor at 464 nm. The ratio of the oscillator strength at 363 nm to the oscillator strength at 464 nm for the V complex is 0.83. At the same time, the Raman cross section for pyridine at the shorter wavelength is estimated to be greater by a factor of 2, as shown in Figure 8, due to the $(\omega - \omega_p)^4$ prefactor in the cross section expression. However, this prefactor is divided out in defining the enhancement factor, so our overall conclusion is that the enhancement factor maximizes at the longer wavelength (464 nm). This result will be amplified if there is more significant damping at shorter wavelength. Thus, we see that the highest enhancement factor is associated with the intraband transition maximum.

Due to the prefactor in the cross section expression, the cross sections for the V-complex of pyridine−Au_{20} are predicted to decrease with increasing wavelength (see Figure 8). At 632.8 nm, the scattering factors are smaller than the scattering factors

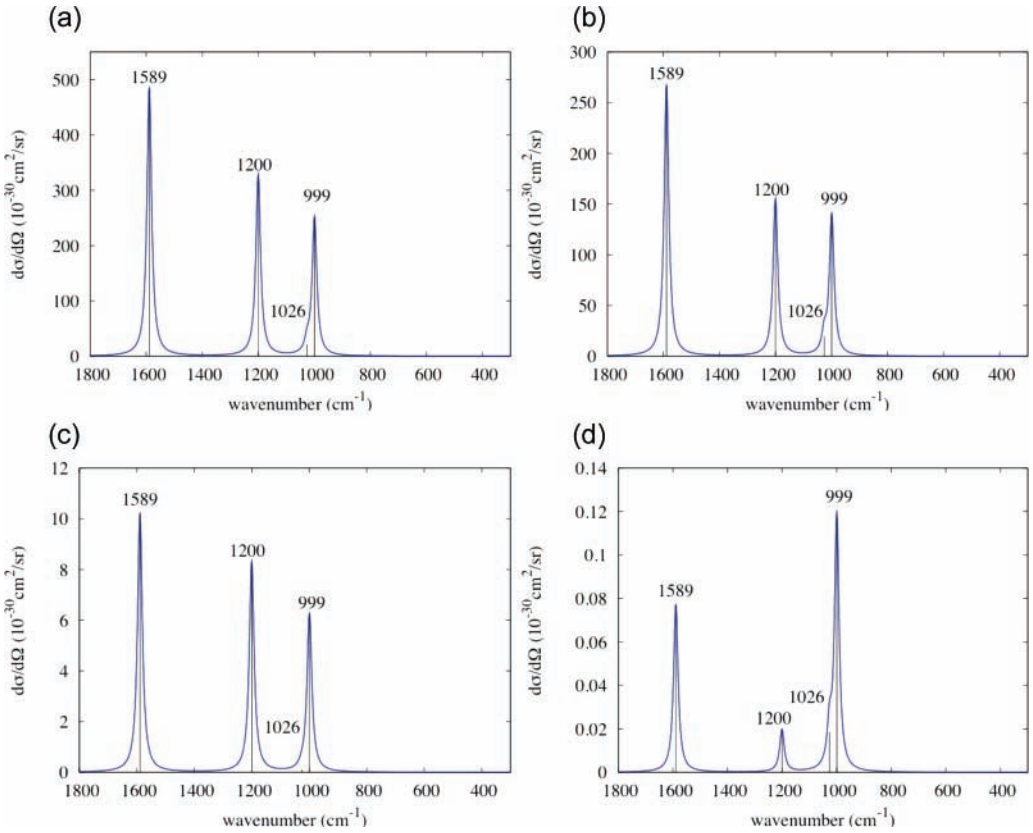

Figure 8. Calculated resonant Raman spectra of four prominent modes of the V-complex of pyridine−Au_{20} as a function of excitation wavelength (a) 363 nm, (b) 464 nm, (c) 632.8 nm, and (d) 1064 nm.

from the 464 nm calculations by a factor of 5, which means that the enhancement at this wavelength is 10^2-10^3 relative to the static pyridine intensity. The appearance of the resonant Raman spectrum is qualitatively similar for excitations at 632.8, 464, and 362 nm. This is as expected, as the electromagnetic enhancement should yield the same enhancement factors for the modes. However, the relative intensities of the peaks in the spectrum computed at an excitation wavelength of 1064 nm are similar to the relative intensities of the peaks in the static Raman spectrum for the V-complex. The enhancement factor at this wavelength is a factor of 2 greater than the static V enhancement factor. The pyridine−Au_{20} complex has no excitations at this low energy, and thus, this excitation wavelength is not resonant with any electronic transitions.

Conclusions

In this study, the influence of the metal substrate on the surface-enhanced Raman scattering of pyridine has been examined. The absorption spectrum of Au_{20} differs from the absorption spectrum of Ag_{20} as a direct consequence of relativistic effects. The gold absorption spectrum contains lower energy maxima, and the oscillator strength is divided among many transitions, resulting in a weaker peak oscillator strength, broader imaginary polarizability maximum, and overall smaller Raman enhancements. This reduction in SERS enhancement for gold relative to silver is similar to what has been observed in experiments on gold nanoparticles.[53] Other differences between gold and silver are that pyridine binds more strongly to gold and the vertex configuration is more strongly bound than the surface configuration. The charge-transfer states are weak and not well separated from metal−metal transitions.

For the gold complexes, the trigonal ring breathing mode has a small intensity relative to the symmetric ring breathing mode. In contrast to silver, the vertex orientation rather than the surface orientation for the gold cluster has a greater overall enhancement factor. Also, the surface configuration has a smaller enhancement factor for gold than for silver. The enhancement factors show a wavelength dependence that is similar to the absorption spectrum. As for silver, the primary enhancement mechanism is the electromagnetic enhancement, with a small contribution from the chemical enhancement.

The relative importance of vertex and surface contributions to the enhancements in practical applications will depend on surface coverage, and in general one expects much larger populations of surface complexes compared to vertex complexes. Thus, the experimental spectra can still be dominated by surface complexes, and there is evidence in the comparison with experiment that this is the case. There is also evidence in the comparison with experiment that our model of a single pyridine interacting with a Au_{20} cluster overestimates the chemical interaction between pyridine and gold, presumably because of differences in coverage compared to the experiments.

Acknowledgment. The authors thank Lasse Jensen and Linlin Zhao for helpful discussions. This work was supported by NSF Grant CHE-0550497 and the Air Force Office of Scientific Research. Some of the calculations were performed with supercomputers at the Environmental Molecular Sciences Laboratory, a national scientific user facility sponsored by the U.S. Department of Energy's (DOE's) Office of Biological and Environmental Research and located at Pacific Northwest National Laboratory, operated for DOE by Battelle.

Supporting Information Available: Optimized geometries and normal modes for the structures considered in this work. This material is available free of charge via the Internet at http://pubs.acs.org.

References and Notes

(1) Fleischmann, M.; Hendra, P. J.; McQuillan, A. J. *Chem. Phys. Lett.* **1974**, *26*, 163.
(2) Jeanmaire, D. L.; Van, Duyne, R. P. *J. Electroanal. Chem.* **1977**, *84*, 1.
(3) Albrecht, M. G.; Creighton, J. A. *J. Am. Chem. Soc.* **1977**, *99*, 5215.
(4) Nie, S.; Emory, S. R. *Science* **1997**, *275*, 1102.
(5) Kneipp, K.; Wang, Y.; Kneipp, H.; Perelman, L. T.; Itzkan, I.; Dasari, R. R.; Feld, M. S. *Phys. Rev. Lett.* **1997**, *78*, 1667.
(6) Michaels, A. M.; Nirmal, M.; Brus, L. E. *J. Am. Chem. Soc.* **1999**, *121*, 9932.
(7) Zuo, C.; Jagodzinski, P. W. *J. Phys. Chem. B* **2005**, *109*, 1788.
(8) Wu, D.-Y.; Duan, S.; Ren, B.; Tian, Z.-Q. *J. Raman Spec.* **2005**, *36*, 533.
(9) Zhang, C.; He, Y.; Cheng, H.-P.; Xue, Y.; Ratner, M. A.; Zhang, X.-G.; Krstic, P. *Phys. Rev. B* **2006**, *73*, 125445.
(10) Mucic, R. C.; Storhoff, J. J.; Mirkin, C. A.; Letsinger, R. L. *J. Am. Chem. Soc.* **1998**, *120*, 12674.
(11) Xu, X.; Rosi, N. L.; Wang, Y.; Huo, F.; Mirkin, C. A. *J. Am. Chem. Soc.* **2006**, *128*, 9286.
(12) Schaaff, T. G.; Whetten, R. L. *J. Phys. Chem. B* **2000**, *104*, 2630.
(13) Boyen, H.-G.; Kästle, G.; Weigl, F.; Koslowski, B.; Dietrich, C.; Ziemann, P.; Spatz, J. P.; Riethmüller, S.; Hartmann, C.; Möller, M.; Schmid, G.; Garnier, M. G.; Oelhafen, P. *Science* **2002**, *297*, 1533.
(14) Haruta, M.; Yamada, N.; Kobayashi, T.; Iijima, S. *J. Catal.* **1989**, *115*, 301.
(15) Valden, M.; Lai, X.; Goodman, D. W. *Science* **1998**, *281*, 1647.
(16) Olson, R. M.; Varganov, S.; Gordon, M. S.; Metiu, H.; Chretien, S.; Piecuch, P.; Kowalski, K.; Kucharski, S. A.; Musial, M. *J. Am. Chem. Soc.* **2005**, *127*, 1049.
(17) Han, Y.-K. *J. Chem. Phys.* **2006**, *124*, 024316.
(18) Walker, A. V. *J. Chem. Phys.* **2005**, *122*, 094310.
(19) Häkkinen, H.; Yoon, B.; Landman, U.; Li, X.; Zhai, H.-J.; Wang, L.-S. *J. Phys. Chem. A* **2003**, *107*, 6168.
(20) Li, J.; Li, X.; Zhai, H.-J.; Wang, L.-S. *Science* **2003**, *299*, 864.
(21) Zhang, H.-F.; Stender, M.; Zhang, R.; Wang, C.; Li, J.; Wang, L.-S. *J. Phys. Chem. B* **2004**, *108*, 12259.
(22) Arenas, J. F.; Soto, J.; López-Tocón, I. *J. Chem. Phys.* **2002**, *116*, 7207.
(23) Johansson, P. *Phys. Chem. Chem. Phys.* **2005**, *7*, 475.
(24) Vivoni, A.; Birke, R. L.; Foucault, R.; Lombardi, J. R. *J. Phys. Chem. B* **2003**, *107*, 5547.
(25) Wu, D. Y.; Hayashi, M.; Lin, S. H.; Tian, Z. Q. *Spectrochim. Acta A* **2004**, *60*, 137.
(26) Wu, D.-Y.; Ren, B.; Xu, X.; Liu, G.-K.; Yang, Z.-L.; Tian, Z.-Q. *J. Chem. Phys.* **2003**, *119*, 1701.
(27) Aroca, R. F.; Clavijo, R. E.; Halls, M. D.; Schlegel, H. B. *J. Phys. Chem. A* **2000**, *104*, 9500.
(28) Cardini, G.; Muniz-Miranda, M. *J. Phys. Chem. B* **2002**, *106*, 6875.
(29) Pandey, P. K. K.; Schatz, G. C. *Chem. Phys. Lett.* **1982**, *88*, 193.
(30) Pandey, P. K. K.; Schatz, G. C. *J. Chem. Phys.* **1983**, *80*, 2959.
(31) Corni, S.; Tomasi, J. *J. Chem. Phys.* **2002**, *116*, 1156.
(32) Jensen, L.; Autschbach, J.; Schatz, G. C. *J. Chem. Phys.* **2005**, *122*, 224115.
(33) Jensen, L.; Zhao, L. L.; Autschbach, J.; Schatz, G. C. *J. Chem. Phys.* **2005**, *123*, 174110.
(34) Jensen, L.; Schatz, G. C. *J. Phys. Chem. A* **2006**, *110*, 5973.
(35) Zhao, L.; Jensen, L.; Schatz, G. C. *J. Am. Chem. Soc.* **2006**, *128*, 2911.
(36) Zhao, L. L.; Jensen, L.; Schatz, G. C. *Nano Lett.* **2006**, *6*, 1229.
(37) te Velde, G.; Bickelhaupt, F. M.; Baerends, E. J.; Fonseca, Guerra, C.; van Gisbergen, S. J. A.; Snijders, J. G.; Ziegler, T. *J. Comp. Chem.* **2001**, *22*, 931.
(38) Becke, A. D. *Phys. Rev. A* **1988**, *38*, 3098.
(39) Perdew, J. P. *Phys. Rev. B* **1986**, *33*, 8822.
(40) Neugebauer, J.; Hess, B. A. *J. Chem. Phys.* **2003**, *118*, 7215.
(41) van Lenthe, E.; Baerends, E. J.; Snijders, J. G. *J. Chem. Phys.* **1993**, *99*, 4597.
(42) http://www.scm.com/Doc/Doc2006.01/Welcome.html
(43) Krykunov, M.; Banerjee, A.; Ziegler, T.; Autschbach, J. *J. Chem. Phys.* **2005**, *122*, 074105.
(44) Jensen, L.; Schatz, G. C. to be published.
(45) Collings, B. A.; Athanassenas, K.; Lacombe, D.; Rayner, D. M.; Hackett, P. A. *J. Chem. Phys.* **1994**, *101*, 3506.
(46) Wu, K.; Li, J.; Lin, C. *Chem. Phys. Lett.* **2004**, *388*, 353.
(47) Xie, R.-H.; Bryant, G. W.; Zhao, J.; Kar, T.; Smith, V. H., Jr. *Phys. Rev. B* **2005**, *71*, 125422.
(48) Taylor, K. J.; Pettiette-Hall, C. L.; Cheshnovsky, O.; Smalley, R. E. *J. Chem. Phys.* **1992**, *96*, 3319.
(49) Fonseca Guerra, C.; Handgraaf, J.-W.; Baerends, E. J.; Bickelhaupt, F. M. *J. Comp. Chem.* **2004**, *25*, 189.
(50) Dreuw, A.; Head-Gordon, M. *J. Am. Chem. Soc.* **2004**, *126*, 4007.
(51) Katayama, K.; Shibamoto, K.; Sawada, T. *Chem. Phys. Lett.* **2001**, *345*, 265.
(52) Note: A factor of 10/45 was omitted from the cross section intensities reported in ref 35. The relative enhancement factors are unchanged, however.
(53) Schatz, G. C. In *Surface Enhanced Raman Scattering*; Chang, R. K., Furtak, T. E., Eds.; Plenum: New York, 1982.